

Robust Automated Thalamic Nuclei Segmentation using a Multi-planar Cascaded Convolutional Neural Network

Submitted to Magnetic Resonance in Medicine, December 2019

Mohammad S Majdi¹, Mahesh B Keerthivasan^{2,5}, Brian K Rutt³, Natalie M Zahr⁴,
Jeffrey J Rodriguez¹, Manojkumar Saranathan^{1,2}

¹Department of Electrical and Computer Engineering, University of Arizona, Tucson, AZ, ²Department of Medical Imaging, University of Arizona, Tucson, AZ, ³Department of Radiology, Stanford University, Stanford, CA, ⁴Department of Psychiatry and Behavioral Sciences, Stanford University, Stanford, CA, ⁵Siemens Healthcare USA, Tucson, AZ

ABSTRACT

Purpose: To develop a fast, accurate, and robust convolutional neural network (CNN) based method for segmentation of thalamic nuclei.

Methods: A cascaded multi-planar scheme with a modified residual U-Net architecture was used to segment thalamic nuclei on clinical datasets acquired using the white-matter-nulled Magnetization Prepared Rapid Gradient Echo (MPRAGE) sequence. A single network was optimized for healthy controls and disease types (multiple sclerosis, essential tremor) and magnetic field strengths (3T and 7T). Another network was developed to use conventional MPRAGE data. Clinical utility was assessed by comparing a cohort of MS patients to healthy subjects.

Results: Segmentation of each thalamus into 12 nuclei was achieved in under 4 minutes. For 7T WMn-MPRAGE, the proposed method outperformed current state-of-the-art with statistically significant improvements in Dice ranging from 1.2% to 5.3% for MS and from 2.6% to 38.8% for ET patients. Comparable accuracy (Dice/VSI) was achieved between 7T and 3T data, attesting to the robustness of the method. For conventional MPRAGE, Dice of > 0.7 was achieved for larger nuclei and > 0.6 for the smaller nuclei. Atrophy of five thalamic nuclei and the whole thalamus was observed for MS patients compared to healthy control subjects, after controlling for intracranial volume and age ($p < 0.004$).

Conclusion: The proposed segmentation method is fast, accurate, and generalizes across disease types and field strengths and shows great potential for improving our understanding of thalamic nuclei involvement in neurological diseases and healthy aging.

KEYWORDS

Deep learning, convolutional neural network, transfer learning, thalamic nuclei segmentation

INTRODUCTION

The thalamus is a deep brain gray matter structure that relays information between various subcortical areas and the cerebral cortex¹ and plays a critical role in regulating sleep, consciousness, arousal, and awareness.²⁻⁴ It is subdivided into multiple nuclei with varying functions. Thalamic involvement has been reported in schizophrenia^{5,6}, alcohol use disorder^{7,8}, Parkinson's disease⁹, multiple sclerosis (MS)¹⁰, and Alzheimer's disease¹¹. These pathologies affect different thalamic nuclei and therefore, accurate volumetry of thalamic nuclei can be very useful for tracking disease progression and treatment efficacy.^{11,12} An emerging use of thalamic nuclei segmentation is in the treatment of essential tremor (ET) using deep brain stimulation.¹³⁻¹⁵ Fast and accurate localization of the ventral intermediate (VIM) nucleus, whose abnormal electrical activity has been implicated in ET, can help improve the success rate of deep brain stimulation surgery and high intensity focused ultrasound treatments of ET.¹⁶

Manual delineation of thalamic nuclei from in-vivo scans is very tedious and requires specialized knowledge.^{17,18} Due to low intra-thalamic contrast¹⁹, thalamic nuclei are not easily distinguishable in conventional T1 or T2 weighted magnetic resonance images. As a result, most structural MRI based automated methods have only segmented the whole thalamus as part of subcortical brain segmentation.²⁰⁻²⁴ Fischl et al.²⁰ used a voxel-wise probabilistic atlas of anatomy and MRI intensities to segment the brain into 15 subcortical structures including the left and right thalamus. This method is currently available as part of the FreeSurfer software.²¹ Patenaude et al.²² used active shape and appearance models along with a Bayesian framework, to create a probabilistic relation between shape and intensity of images. An implementation of this method (FIRST) is available as part of the FSL software package.²⁵

Advanced neuroimaging techniques such as susceptibility-weighted imaging (SWI)²⁶ can provide better intra-thalamic contrast, compare to conventional T1 and T2 weighted MRI and have been used for segmentation of thalamic nuclei at 7T.^{27,28}

However, they are time consuming and have been successful in segmenting mainly the VIM nucleus used in neurosurgical applications. Diffusion Tensor Imaging (DTI) based methods have been more popular and use either local or global properties of the diffusion tensor to segment thalamic nuclei. Behrens et al.²⁹ used tractography of cortical projections to the thalamus to segment thalamic regions, but this method requires precise knowledge of neuroanatomy to identify the relevant cortical regions. More automated, computationally efficient methods have been proposed that use k-means clustering of the dominant diffusion orientation to achieve thalamic parcellation.^{30–32} The most consistent DTI method³³ to date, uses spherical harmonic decomposition based orientation distribution functions to achieve robust segmentation of 7 thalamic nuclei. However, the low spatial resolution of echo-planar imaging which underlies DTI and the predominance of gray matter in the thalamus which results in low anisotropy make these DTI-based methods suboptimal³⁴, often resulting in segmentation of only the larger thalamic groups.

Other attempts to segment thalamic nuclei have relied on supervised machine learning techniques. Stough et al.³⁵ used a random forest classifier to combine features extracted from DTI along with traditional T1-weighted MRI to segment the four large thalamic groups along with the lateral geniculate nucleus (LGN) and medial geniculate nucleus (MGN). Glaister et al.³⁶ extended the above approach by proposing a cascaded random forest classifier that makes use of DTI features along with atlas based nuclei priors to first detect the thalamus followed by nuclei segmentation.

Recently, high spatial resolution structural MRI has been investigated for thalamic nuclei segmentation. The most widely used T1-weighted structural MRI sequence is the Magnetization-Prepared Rapid Gradient Echo (MPRAGE), where the cerebrospinal fluid (CSF) is nulled. We refer to this method as CSFn-MPRAGE in the rest of the document. Iglesias et al.²⁴ proposed a probabilistic atlas constructed using manual delineation of 26 thalamic nuclei per thalamus on six autopsy specimens and used Bayesian inference to segment 3T MPRAGE images into 26 nuclei per side.^{37,38} However, this method requires multiple hours for the segmentation of one subject and has not been validated against manual segmentation.²⁴ Variants of the MPRAGE sequence have been proposed to better visualize the intra-thalamic structures.^{39,40} Su et al.³⁴ used a white matter nulled MPRAGE (WMn-MPRAGE) sequence that is

optimized for intra-thalamic contrast¹⁹ in conjunction with an atlas-based technique called thalamus optimized multi-atlas (THOMAS), to segment the thalamus into 12 nuclei. However, the performance of this atlas-based method hinges on the accuracy of a computationally expensive registration step.^{24,41} Because of anatomical variability, the choice of an atlas that could be easily generalizable tends to be hard.⁴² Moreover, this method has only been validated on specialized 7T WMn-MPRAGE data. Liu et al.⁴³ segmented thalamic nuclei from 3T T1 weighted MRI data using an atlas developed from multiple MPRAGE and SWI sequences acquired at 7T. A multi-atlas label fusion and statistical shape modeling algorithm was used to transfer this from 7T to 3T.

In recent years, deep learning has become a popular tool for detection and segmentation of medical images.^{44–49} Convolutional neural networks (CNNs) are a class of deep learning techniques that use convolutional kernels to capture the non-linear mapping between an input image and its segmentation labels. Unlike atlas based segmentation techniques, CNNs do not depend on image registration and manual feature extraction.⁵⁰ While many studies have explored the advantages of using CNNs for subcortical segmentation^{44,47,51,52}, these are limited to the whole thalamus. Due to paucity of training data and the high computational and memory requirements of 3D analysis, most proposed methods make use of 2D CNNs.⁵¹ However, the use of 2D networks does not fully exploit the anatomical information present in 3D volumetric MRI data. Alternatively, multi-planar techniques that make use of 2D CNNs along the three orthogonal planes have been shown^{47,53–55} to improve segmentation performance with lower computational cost than a full 3D analysis. Transfer learning techniques have also been investigated to mitigate the problem of lack of sufficient training data.⁵⁶

In this work, we propose a cascaded multi-planar scheme using a modified residual U-Net for thalamic nuclei segmentation using images from the WMn-MPRAGE sequence^{19,57} and validate our technique in both healthy subjects and patients with MS and ET as well as using data from 3T and 7T scanners. We further extend this framework to segment thalamic nuclei from conventional MPRAGE acquisition. Lastly, we demonstrate a clinical application of thalamic nuclei segmentation for patients with MS.

METHODS

Proposed Architecture

The proposed modified residual U-Net architecture for thalamic nuclei segmentation is shown in Figure 1 (top panel). The U-Net uses a contracting (encoder) layer and an expanding (decoder) layer for multi-resolution feature extraction and synthesis. To improve the convergence performance and reduce overfitting, batch normalization⁵⁸ and dropout⁵⁹ layers were added to a conventional U-Net⁶⁰ (mU-Net). Residual convolutional blocks⁶¹ were added to mitigate the problem of vanishing and exploding loss function gradients. We call this resulting architecture modified residual U-Net (mRU-net). Each convolutional block consists of 2D convolution units followed by a batch normalization⁵⁸ and a leaky rectified linear unit⁶² (leakage factor 0.1). A 1x1 convolution with a softmax activation function was used to map the final feature maps into the desired number of classes, generating a probability map for each class.

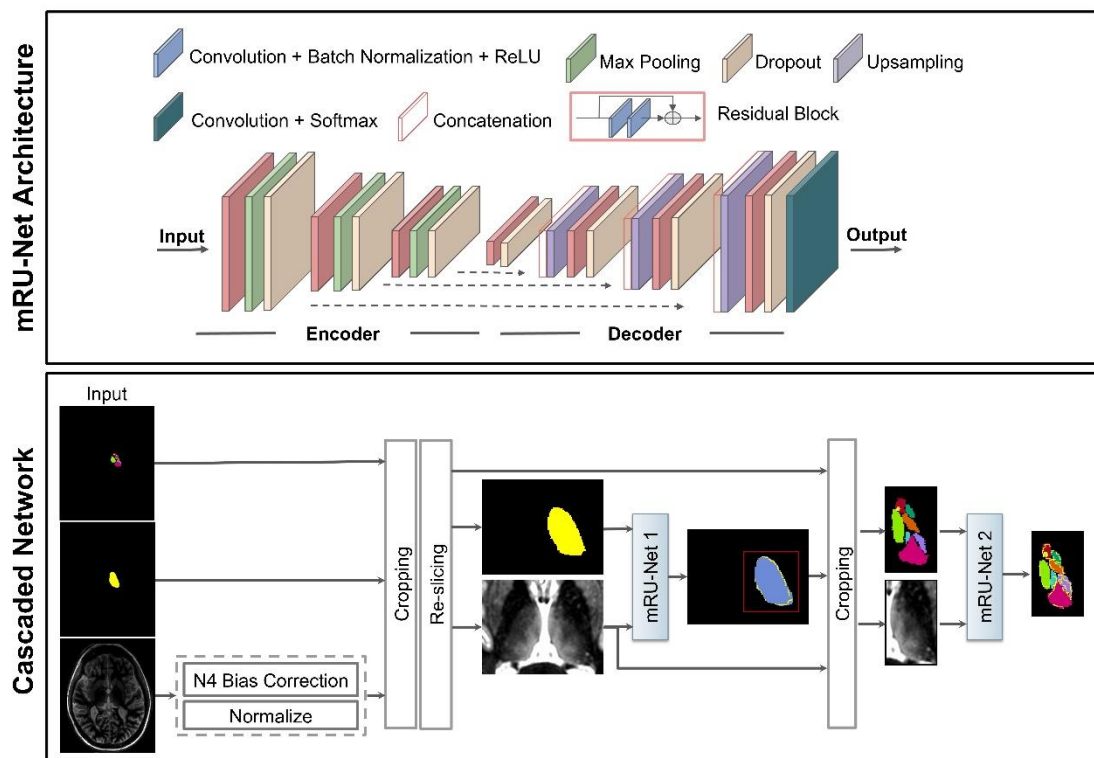


Figure 1: The proposed CNN architecture with normalization and residual blocks added to a U-Net (Top panel). Following preprocessing, mRU-Net1 is trained to predict the whole thalamus. The output of this network is used to find a bounding box that encompasses the left thalamus (shown in red). The cropped inputs are then fed to a second network (mRU-Net2) to predict the thalamic nuclei (Bottom panel).

A two-step cascaded approach was used that first segments the whole thalamus and then segments different nuclei as shown in Figure 1 (bottom panel). A network was trained to first detect the left thalamus from the pre-processed input images (see preprocessing section for details) and generate a thalamus bounding box. The bounding box was used to further crop the inputs before being fed to the second network. Segmentation of the right thalamus and right thalamic nuclei was achieved by flipping the input images in the left-right direction and using them as test cases.

2D CNNs cannot fully utilize the spatial information present in an isotropic resolution 3D MRI volume. However, due to the limitation in the number of labeled datasets available, training a generalizable 3D CNN which can exploit the 3D structure is infeasible. In order to overcome this limitation, a hybrid multi-planar approach as shown in Figure 2 is proposed. The preprocessed 3D volumes are reformatted into three orthogonal planes (axial, coronal, and sagittal) and used to train three cascaded 2D networks to take advantage of the complementary information from each plane. The final segmentations are reformatted to the original plane and fused using voxel-wise majority voting.

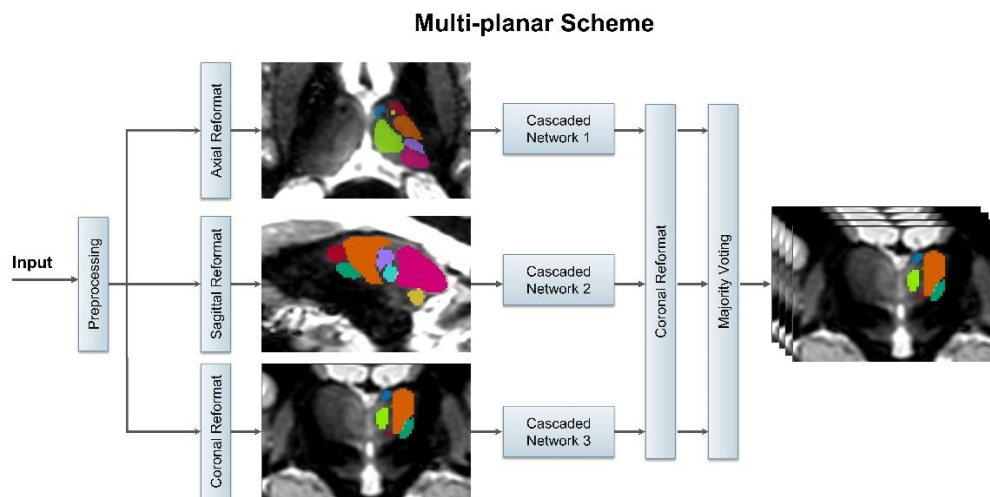


Figure 2: Proposed Multi-planar Scheme- the 3D input images are reformatted to sagittal, coronal, and axial planes and used to train three separate cascaded mRU-Nets. The predictions from the three 2D networks are fused using majority voting to generate the final thalamus segmentation mask.

The network used for segmentation of the whole thalamus used a log-Dice loss function along with sigmoid activation. For the subsequent multi-class thalamic nuclei segmentation network, we investigated two different loss functions: a) weighted cross-

entropy loss and b) logarithm of Dice. The multi-class weighted cross-entropy loss is defined as

$$L1 = - \sum_{i=0}^{C-1} w_i (q_i \log(p_i) + (1 - q_i) \log(1 - p_i)) \quad (1)$$

where C is the number of classes (2 for the whole-thalamus network and 13 for the subsequent nuclei segmentation network), $p_i = \exp(\hat{y}_i) / \sum_{k=0}^{C-1} \exp(\hat{y}_k)$ is the posterior for class i obtained by applying the softmax function to the network's final feature maps \hat{y}_i , w_i represents the weight for class i , and q_i is the ground truth for class i .

The weights for each class were computed as:

$$w_i = \frac{N}{|B_i|} \quad (2)$$

where N and $|B_i|$ are the total number of voxels and the number of foreground voxels corresponding to nucleus i in the 3D input's manual label (B_i) respectively.

Since Dice coefficient based loss functions have been shown to improve performance compared to cross-entropy⁶³, we use the following loss function defined as:

$$L2 = \frac{1}{C} \sum_{i=0}^{C-1} \log(\text{Dice}(A_i, B_i)) \quad (3)$$

$$\text{Dice}(A_i, B_i) = \frac{2|A_i \cap B_i|}{|A_i \cup B_i|} \quad (4)$$

where A_i and B_i are the predicted and manual segmentations for nucleus i respectively and $|\cdot|$ is the $l1$ norm. Note that the different classes are implicitly weighted when using a Dice-based loss function.^{64,65}

Network Training

The networks were trained using the Adam optimizer⁶⁶ with 300 epochs and a batch size of 100 for the cascaded and 30 for the non-cascade scheme. Performance of the network was evaluated for the weighted cross entropy and log-Dice loss functions. The number of layers, number of convolutional feature maps, and learning rates were chosen based on hyper-parameter tuning. The learning rate for the WMn-MPRAGE network was set initially to 0.0001 and decreased by a factor of 2 every 20 epochs. In

order to generalize the thalamic segmentation to include conventional CSF-nulled MP-RAGE images, a transfer learning approach was used. This network was initialized with weights from the WMn-MP-RAGE network and retrained on the CSFn-MP-RAGE images. The CSFn-MP-RAGE network was trained with the log-Dice loss function using an Adam optimizer with 300 epochs and a batch size of 100. The learning rate was set to a constant value of 0.001.

Pre- and Post-Processing

All input images were preprocessed by performing N4 bias-field correction and zero mean unit standard deviation normalization. In order to spatially constrain the input images and reduce memory consumption, all images were cropped using an approximate bounding box that encompassed the left and right thalami. A template image was derived from mutual registration and averaging of 20 prior WMn-MP-RAGE datasets as described in Su et al.³⁴ A bounding box that covered both thalami was drawn on this template and warped into the input image space by affine registering the template with the input image. All input images were reformatted to the same imaging plane and resolution (axial with $0.7 \times 0.5 \times 0.7 \text{ mm}^3$). The preprocessing steps are shown in Figure 1 (bottom panel). To ensure enough variability, the training data were augmented using random in-plane rotations of up to $\pm 7^\circ$ in three different planes, creating six new images in each orientation and a net increase in the number of training data by a factor of 18.

Datasets

To evaluate thalamic nuclei segmentation of WMn-MP-RAGE images, data from 40 subjects (13 healthy subjects, 15 patients with MS, and 12 patients with ET), all acquired on a 7T GE scanner were used. The 12 ET patients were rescanned on a 3T GE scanner to investigate the effect of field strength. A separate dataset consisting of 93 WMn-MP-RAGE images from a 3T GE scanner that included patients with alcohol use disorder and healthy control subjects were used just for the purpose of network initialization. Reference labels for this dataset were obtained using the THOMAS algorithm.³⁴ In order to evaluate the segmentation of CSFn-MP-RAGE images, data from 34 subjects (7 healthy subjects, 15 patients with MS, and 12 patients with ET) scanned with both WMn-MP-RAGE and CSFn-MP-RAGE pulse sequences on a 7T GE

scanner were used. The pulse sequence parameters for both the WMn-MPRAGE and CSFn-MPRAGE pulse sequences are listed in Supporting Table S1.

Reference labels for WMn-MPRAGE images were generated using manual segmentation of thalamic nuclei, performed by a trained neuroradiologist using the Morel histological atlas⁶⁷ as a guide. Twelve thalamic nuclei including the mammillothalamic tract (MTT) were delineated using freehand spline drawing tools to build the 3D vector-based model of each structure. The delineated nuclei included, the medial group (the mediodorsal nucleus (MD), center median nucleus (CM), habenular nucleus (Hb)), posterior group (the pulvinar (Pul), medial geniculate nucleus (MGN), lateral geniculate nucleus (LGN)), lateral group (the ventral posterolateral nucleus (VPL), ventral lateral anterior nucleus (VLa), ventral lateral posterior nucleus (VLp), ventral anterior nucleus (VA)), and the anterior group (the anterior ventral nucleus (AV)), as well as the MTT. Reference labels for CSFn-MPRAGE images were obtained by registering WMn-MPRAGE images to the corresponding CSFn-MPRAGE images and warping the labels using nearest-neighbor interpolation.

Experiments

The network was implemented in Python and Keras⁶⁸ with a TensorFlow backend using an NVIDIA P100 GPU with 16 GB GDDR5 RAM. The effect of network initialization was investigated by training the network using random initialization as well as initialization from another segmentation network that was developed using data from a 3T GE scanner along with THOMAS reference labels as described above in **Datasets**. In order to evaluate the utility of the proposed cascaded approach, a non-cascaded axial network was also trained using the same data. The effect of residual blocks on segmentation performance was evaluated by training two conventional U-Net architectures, with and without the residual blocks. Finally, the multi-planar approach was evaluated by training three separate networks and combining the results using majority voting. In the multi-planar approach, after a series of hyperparameter tuning, the number of feature maps on the first layer was set to 40, 30 and 20 for the sagittal, coronal and axial networks respectively. The number of feature maps in each succeeding layer was increased by a factor of two as proposed in the conventional U-Net⁶⁰. To pick the optimal network architecture and features, we

used 12 subjects (4 control, 4 MS, 2 7T ET, 2 3T ET) for testing and the remaining for training.

To evaluate the segmentation performance of the final optimized WMn-MPRAGE and CSFn-MPRAGE networks, a full 4-fold cross validation was performed. In each fold, 75% of the data was used for training and the remaining 25% was used for testing. All data were equally distributed with respect to control/disease type between each fold (e.g. in the WMn-MPRAGE network, the first fold had 3 control, 4 MS, and 6 ET subjects for testing and 10 control, 11 MS, and 18 ET subjects for training). Note that for the ET cases, data from subjects acquired from both 3T and 7T were used simultaneously to impart robustness to field strength. In order to compare the segmentation performance of the proposed CNN, the THOMAS algorithm was used to segment thalamic nuclei from WMn-MPRAGE images. The ability of the network to detect the right thalamic nuclei was tested using left-right flipped images of healthy subjects in WMn-MPRAGE data. A two-tailed paired t-test was performed between the volumes of left and right thalamic nuclei predictions to validate the segmentation performance. The effect of transfer learning on segmenting CSFn-MPRAGE images was investigated by systematically freezing and fine-tuning different layers of the WMn-MPRAGE network.

Performance evaluation metrics

The final prediction accuracy was evaluated with respect to the manual delineations using the following metrics: Dice coefficient⁶⁹, volume similarity index (VSI)³⁴, and Hausdorff distance (HD)⁷⁰.

The Dice coefficient shown in Eq. (4) measures overlap between the manual segmentation and the estimated segmentation computed by the network. A Dice coefficient of 1 indicates perfect segmentation while a score of 0 indicates no overlap. The volumetric similarity index is defined as a ratio of the absolute volume difference and sum of individual volumes:

$$\text{VSI}(A, B) = \frac{1}{C} \sum_{i=0}^{C-1} \left(1 - \frac{||A_i| - |B_i||}{|A_i| + |B_i|} \right) \quad (5)$$

where A_i and B_i are the predicted and manual segmentations for nucleus i .

Hausdorff distance measures the distance between border voxels of the estimated segmentation and the border voxels of the manual segmentation⁷¹:

$$\text{HD}(A, B) = \frac{1}{C} \sum_{k=0}^{C-1} \max(h(A_i, B_i), h(B_i, A_i)) \quad (6)$$

where $h(A_i, B_i)$ is the directed Hausdorff distance defined as

$$h(A_i, B_i) = \max_{a \in A_i} \min_{b \in B_i} \|a - b\|_2 \quad (7)$$

where $\|\cdot\|$ is the Euclidean norm.

The posterior predictions from the network were binarized using thresholds computed from a precision-recall curve as shown in Supporting Figure S1. The threshold (0.7) was determined by finding the tradeoff between values of precision and recall that would correspond to the lowest false positive and false negative.

Clinical analysis

Statistical analysis was performed to investigate the effect of MS on specific thalamic nuclei. The left and right thalamic nuclei were segmented from 7T WMn-MPRAGE data acquired on 15 MS patients and 13 healthy subjects. The segmentation masks were used to compute the average volumes for left and right thalamic nuclei. The thalamic nuclei volumes were corrected for effect of parallel imaging, intracranial volume, and age using multiple linear regression. A two-tailed t-test was performed between the thalamic nuclei volumes of healthy subjects and MS patients with a Bonferroni corrected p-value of $0.05/13=0.00384$ (to account for multiple comparisons of the 11 nuclei, MTT, and whole thalamus).

RESULTS

The overall training time required on an NVIDIA P100 GPU card for the whole thalamus and multi-class thalamic nuclei segmentation was 1 hour and 1.5 hours respectively for a single plane (axial). The cumulative required training time for the final multi-planar scheme, that includes training of three separate networks for axial, coronal, and sagittal orientations was 7.5 hours. The time required for pre-processing and segmentation of each subject in the testing phase of the final multi-planar scheme was 3 min. and 1 min. respectively. The performance of the mRU-Net model investigated using two different loss functions (weighted BCE loss and logarithm of

Dice) on the WMn-MPRAGE dataset is shown in Supporting Figure S1. The use of Dice loss function improved the validation Dice by 9.2% whilst reducing the convergence time by 43%. As a result, the Dice loss function was used for all further experiments.

Table 1 shows the effect of different networks on the WMn-MPRAGE dataset. Note that the thalamic nuclei are arranged in descending order of size with the smaller nuclei (<300 mm³) shaded in grey. This format is used for all subsequent tables. The cascaded network with residual blocks (column 4) showed statistically significant improvement (denoted by †) over the non-cascaded network (column 3) for Pul, VLp, MD, AV, and VLa nuclei. The use of a cascaded scheme reduced the required memory for training by up to 86% enabling the use of augmented data during the training process. Further, it reduced the time of convergence by 83% (74% in the number of epochs, and 35% in time per epoch) in presence of augmented data in comparison to a non-cascaded algorithm without augmented data. Adding residual blocks increased the number of trainable parameters by 21% and the required memory for training by 24%. However, it improved the overall accuracy, showing a statistically significant improvement (denoted by *) for full thalamus, Pul, VA and Hb nuclei (column 4) in comparison to a similar network without residual blocks (column 2). Finally, using a multi-planar network (column 5) as opposed to a single-plane network (column 4), showed a statistically significant improvement (denoted by ‡) for Pul, VLp, VPL, AV, and CM nuclei, while increasing the overall training time by a factor of three.

Table 1: Comparison of performance (Dice, training time, memory, network parameters) for different networks on WMn-MPRAGE

Network	cascade mU-Net	non-cascade mRU-Net	cascade mRU-Net	MP cascade mRU-Net
THALAMUS	0.90	0.92	0.92*	0.92
Pul	0.84	0.85	0.86**†	0.87‡
VLp	0.78	0.75	0.78†	0.79‡
MD-Pf	0.85	0.84	0.86†	0.86
VPL	0.67	0.66	0.67	0.70‡
VA	0.69	0.70	0.71*	0.71
LGN	0.73	0.70	0.73	0.73
AV	0.74	0.72	0.75†	0.77‡
CM	0.71	0.69	0.70	0.74‡
VLa	0.64	0.63	0.65†	0.68
MGN	0.73	0.74	0.74	0.74
MTT	0.71	0.68	0.70	0.72
Hb	0.73	0.77	0.78*	0.79
Training Time	42s / epoch	82s / epoch	52s / epoch	3x(52s / epoch)
Memory Usage	~2.1 GB	+15GB/+9GB	~2.6 GB	~2.5 GB
Total Params	184,113	223,162	223,162	~200,000
Trainable Params	183,313	222,362	222,362	~200,000

* $p < 0.05$ residual vs. non-residual scheme (col 4 vs. col 2)

† $p < 0.05$ cascaded vs. non-cascaded scheme (col 4 vs. col 3)

‡ $p < 0.05$ multi-planar (MP) vs. single-plane scheme (col 5 vs. col 4)

A statistically significant improvement in Dice for two nuclei (VA, and Hb) was observed when the network was initialized using weights from a network trained on 3T WMn-MPRAGE dataset and THOMAS labels compared to random initialization as shown in Supporting Figure S2. Table 2 shows the average Dice for the WMn-MPRAGE network, shown separately for healthy subjects (n=13) and patients with MS (n=15) and ET (n=12). In comparison to the current state-of-the-art method THOMAS, the final results show a significant improvement for ET patients, while showing a slightly higher accuracy (<6% maximum) for control subjects and MS patients. The statistically significant improvements for ET range from 2% for MD to 38% for VLa. Note also the almost identical Dice performance between 3T and 7T for the ET data set ($p > 0.2$ for all nuclei, Table 2 columns 7-8), attesting to the robustness of the method to field strength. Absolute volumes and VSI for different thalamic nuclei for controls, MS, and ET patients are shown in Table 3. It can be seen that the VSI values are quite high for both methods with the CNN showing slightly higher values for the

control cases (VL_a and MGN). A paired t-test between the volumes of left and right thalamic nuclei predictions on healthy control subjects did not show any statistically significant differences indicating comparable segmentation performance for the right thalamic nuclei.

Table 2: Comparison of Dice coefficients for THOMAS vs. proposed CNN-based method for healthy controls, MS, and ET patients for WMn-MPRAGE

		Dice					
Disease	Control 7T		MS 7T		ET 7T		ET 3T
Method	THOMAS (n=13)	CNN (n=13)	THOMAS (n=15)	CNN (n=15)	THOMAS (n=12)	CNN (n=12)	CNN (n=12)
THALAMUS	0.92	0.92	0.92	0.92	0.88	0.90*	0.90
Pul	0.87	0.87	0.85	0.86*	0.84	0.85	0.84
VL_p	0.79	0.80	0.79	0.80	0.75	0.80*	0.79
MD-Pf	0.86	0.87	0.85	0.86	0.83	0.85*	0.85
VPL	0.68	0.72*	0.69	0.71	0.57	0.63*	0.62
VA	0.71	0.76*	0.69	0.72*	0.58	0.66*	0.64
LGN	0.75	0.77	0.71	0.69	0.55	0.51	0.55
AV	0.77	0.80	0.78	0.78	0.64	0.72*	0.72
CM	0.75	0.76	0.74	0.76	0.63	0.64	0.64
VL_a	0.65	0.73*	0.64	0.67	0.47	0.65*	0.66
MGN	0.68	0.74*	0.75	0.76	0.63	0.67*	0.66
MTT	0.67	0.71*	0.69	0.73*	0.67	0.67	0.64
Hb	0.76	0.81*	0.72	0.75	0.76	0.74	0.73

* $p < 0.05$ CNN vs. THOMAS

Figure 3 shows qualitative results from a patient with ET scanned at both 3T and 7T MRI scanners using WMn-MPRAGE. Representative axial and coronal slices with predicted labels overlaid for both the left and right thalamus are shown. The increased SNR and B₁ inhomogeneity in the 7T image (top) can be clearly seen at the edges while the intra-nuclear contrast seems very comparable.

Table 3: Comparison of mean thalamic nuclear volumes (average of left and right) and VSI for THOMAS vs. proposed CNN-based method for healthy controls, MS, and ET patients for WMn-MPRAGE

Disease	Volume (mm ³)				VSI					
	Control 7T	MS 7T	ET 7T	ET 3T	Control 7T		MS 7T		ET 7T	ET 3T
	CNN (n=13)	CNN (n=15)	CNN (n=12)	CNN (n=12)	THOMAS (n=13)	CNN (n=13)	THOMAS (n=15)	CNN (n=15)	CNN (n=12)	CNN (n=12)
THALAMUS	5,933	4,967	4,861	5,103	0.97	0.97	0.98	0.98	0.95	0.96
Pul	1,561	1,181	1,099	1,161	0.96	0.96	0.95	0.95	0.95	0.96
VLp	954	811	871	906	0.97	0.96	0.93	0.94	0.94	0.95
MD-Pf	738	651	627	650	0.94	0.95	0.95	0.96	0.95	0.96
VPL	383	333	297	320	0.90	0.93	0.92	0.93	0.92	0.92
VA	372	327	265	268	0.88	0.90	0.91	0.89	0.93	0.94
LGN	137	111	82	107	0.91	0.92	0.91	0.90	0.80	0.86
AV	172	128	104	120	0.89	0.94	0.93	0.91	0.87	0.94
CM	143	130	79	89	0.91	0.93	0.89	0.90	0.91	0.91
VLa	122	114	104	121	0.81	0.94*	0.87	0.87	0.89	0.92
MGN	97	81	64	79	0.79	0.88*	0.90	0.90	0.84	0.90
MTT	51	56	42	45	0.91	0.89	0.91	0.90	0.88	0.89
Hb	29	24	27	30	0.88	0.90	0.90	0.89	0.92	0.90

* p < 0.05 CNN vs. THOMAS

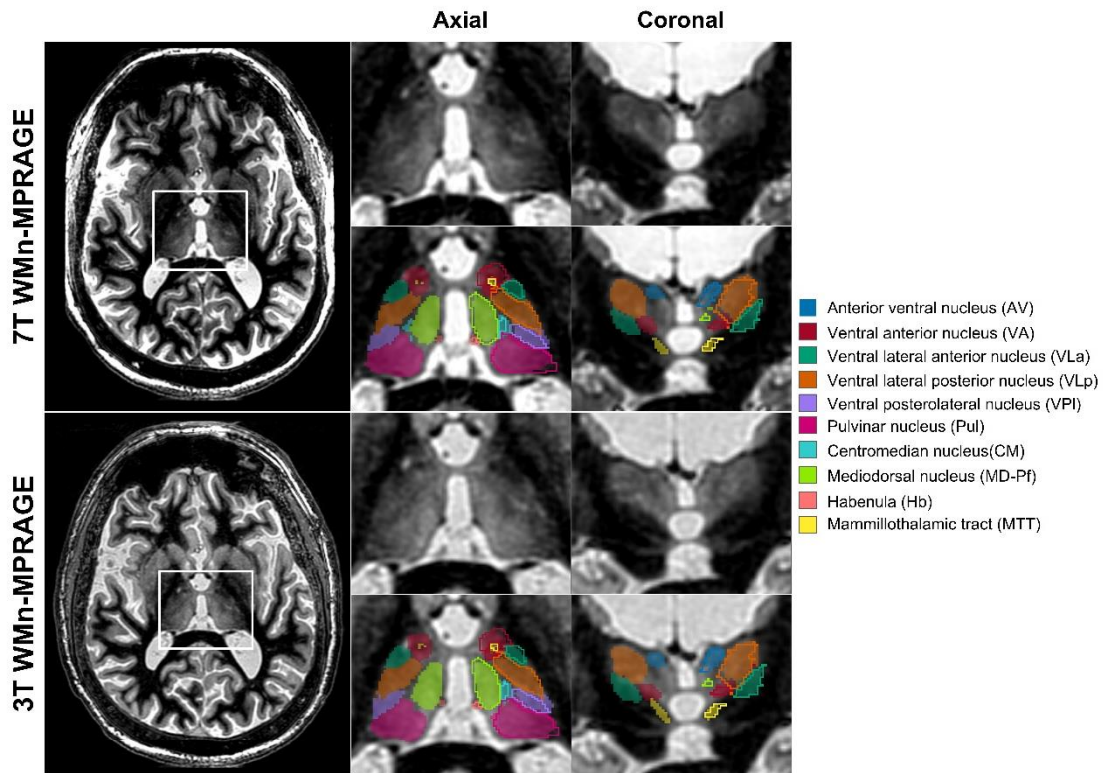


Figure 3: WMn-MPRAGE images from a patient with ET acquired at 7T (top) and 3T (bottom) are shown on the left. The zoomed inset images on the right show representative axial and coronal sections with and without predicted label overlays. The predicted thalamic nuclei masks are almost identical. Note the clear visualization of the MTT and habenula on both sets of images.

A transfer learning approach based on the WMn-MPRAGE segmentation network was used to segment the thalamic nuclei in conventional T1-weighted MPRAGE images. Supporting Table S2 shows different experiments (freezing specific layers and fine-tuning the remaining layers) performed to find the optimum transfer learning approach. Freezing the top layers of the network resulted in improved Dice compared to freezing the bottom layers (5.5% and 4.1% increase for large and small nuclei respectively). Further, freezing the left side of the proposed architecture showed a 4% improvement in Dice in comparison to freezing the right side of the architecture for both large and small nuclei. The best segmentation performance was obtained by freezing the top two left layers and the top right layers of the architecture. However, when compared to full fine tuning of the network, the average Dice from this transfer learning scheme showed a small improvement of 1.35% and 1.59% for large and small nuclei respectively. Therefore, the full fine-tuned network was used for all the subsequent analysis of CSFn-MPRAGE data.

Images from an MS patient acquired using two different contrasts (WMn-MPRAGE and CSFn-MPRAGE) along with their overlaid segmentations are shown in Figure 4. We can clearly see that the network has predicted the thalamic nuclei fairly accurately in the CSFn-MPRAGE image, despite its poor intra-thalamic contrast. For the larger nuclei, Dice values for these two subjects ranged from 0.7-0.93 and 0.70-0.91 for WMn-MPRAGE and CSFn-MPRAGE respectively and for the smaller nuclei, Dice values ranged from 0.71-0.81 and 0.60-0.78 respectively, attesting to comparable network performance.

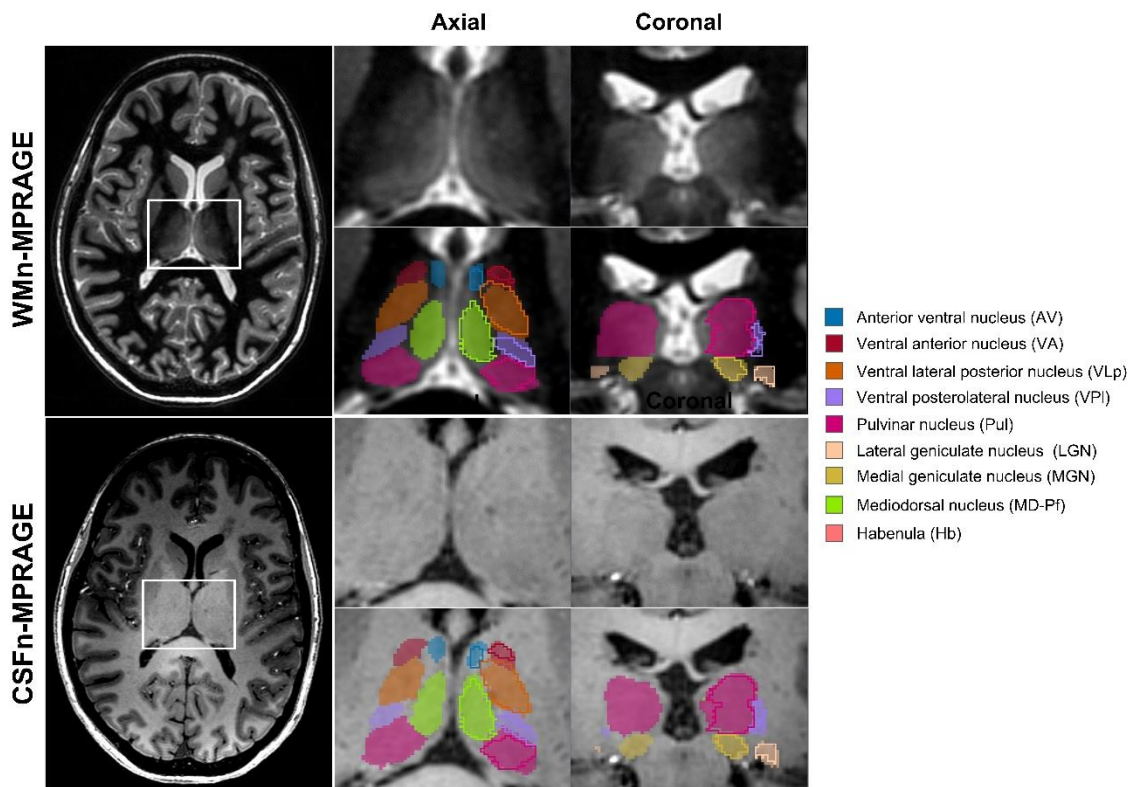


Figure 4: WMn-MPRAGE (top) and CSFn-MPRAGE (bottom) images from a patient with MS acquired at 7T are shown on the left. The zoomed inset images on the right show representative axial and coronal sections with and without predicted label overlays. Note the comparable thalamic nuclei predictions for both cases despite the poor intra-thalamic nuclear contrast in the CSFn-MPRAGE image.

Table 4 shows the average Dice and VSI for CSFn-MPRAGE data (7 healthy subjects, 15 patients with MS and 12 ET). While the Dice values are lower than the corresponding WMn-MPRAGE data especially for the smaller nuclei, the average Dice was 0.77 and 0.63 for large and small nuclei in contrast to 0.82 and 0.7 for the WMn-MPRAGE data. Values of >0.7 were achieved for all large nuclei and >0.6 for all small nuclei (except MTT). Similar results can be observed in terms of VSI with an average VSI of 0.93 and 0.86 for large and small nuclei showing considerable accuracies in comparison to WMn-MPRAGE data with an average VSI of 0.94 and 0.89 for large and small nuclei. Finally, the average Hausdorff distance for healthy controls and MS subjects for WMn-MPRAGE and CSFn-MPRAGE data is shown in Supporting Table S3 with minimal differences between both methods.

Table 4: Comparison of Dice coefficients and VSI for proposed CNN-based method for healthy controls, MS, and ET patients for CSFn-MPRAGE

Disease	Dice			VSI		
	Control 7T (n=7)	MS 7T (n=15)	ET 7T (n=12)	Control 7T (n=7)	MS 7T (n=15)	ET 7T (n=12)
THALAMUS	0.90	0.90	0.90	0.97	0.97	0.96
Pul	0.82	0.82	0.82	0.94	0.94	0.93
VLp	0.76	0.76	0.79	0.96	0.94	0.94
MD-Pf	0.81	0.82	0.83	0.96	0.94	0.95
VPL	0.61	0.63	0.65	0.87	0.89	0.91
VA	0.69	0.69	0.65	0.89	0.90	0.91
LGN	0.66	0.64	0.54	0.89	0.84	0.85
AV	0.73	0.68	0.69	0.91	0.84	0.92
CM	0.62	0.66	0.62	0.87	0.85	0.88
VLa	0.63	0.60	0.62	0.90	0.84	0.88
MGN	0.64	0.69	0.60	0.88	0.87	0.82
MTT	0.40	0.57	0.58	0.68	0.90	0.83
Hb	0.73	0.66	0.68	0.93	0.85	0.84

Figure 5 shows box plots of whole thalamus volumes and volumes of 5 nuclei (AV, VPL, Pul, MGN, and MD) that showed statistically significant reduction in patients with MS compared to healthy subjects. Representative axial and sagittal WMn-MPRAGE sections from an MS patient are shown to the left of the plots, with the nuclei labeled for reference. These results show that our network is capable of performing reliably even in the presence of MS lesions.

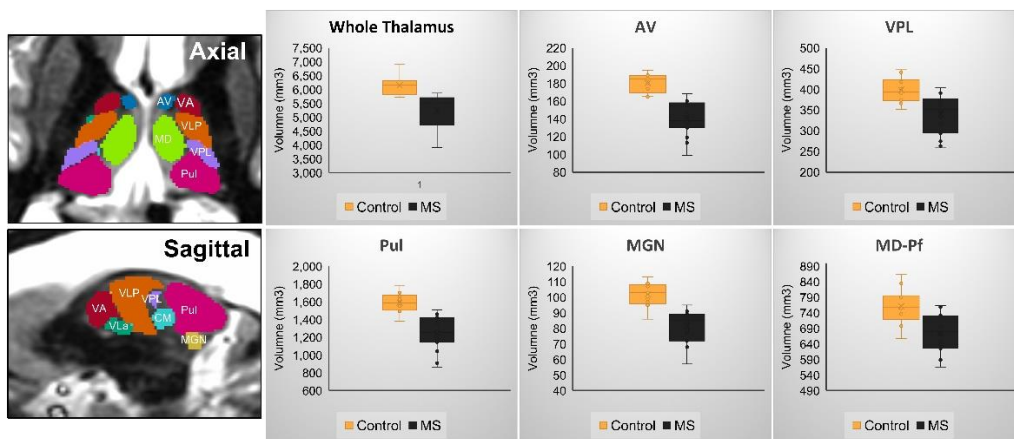


Figure 5: Box plots depicting volumes from whole thalamus and thalamic nuclei that had significantly reduced volumes ($p < 0.00384$) in MS patients compared to healthy subjects are shown on the right. All volumes were corrected for parallel imaging factor, age, and intracranial volume using multi-linear regression. The predicted labels overlaid on WMn-MPRAGE images from an MS patient are shown on the left for axial and sagittal planes.

Figure 6 shows segmentation results of WMn-MPRAGE data acquired from a 3T Siemens scanner (left) and 3T Canon scanner (right). Different vendors use different correction techniques for transmit/receive B_1 homogeneity and filtering, which could result in suboptimal network performance. Our network could accurately segment both cases, attesting to its robustness.

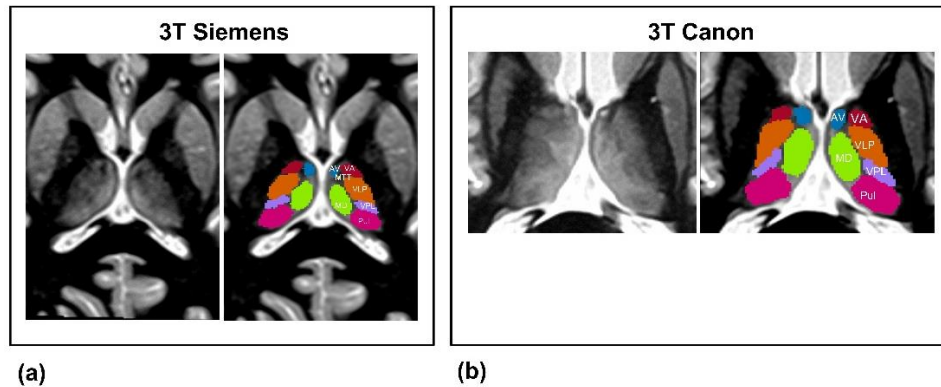


Figure 6: Segmentation results of WMn-MPRAGE acquired from a 3T Siemens scanner (left) and 3T Canon scanner (right) are shown to demonstrate robustness of the method. Note the differently sized bounding boxes.

DISCUSSION

Many studies have explored the use of CNNs in subcortical segmentation^{44,47,51,52} but this is the first work to use CNNs to segment the thalamic nuclei from structural MRI data. A single network for segmentation of WMn-MPRAGE data is introduced for 3T and 7T as well as for healthy controls and patients. The same network also successfully segmented images acquired on different MRI scanners that were not part of the training datasets (Canon, Siemens), attesting to its robustness. Twelve thalamic nuclei including small structures like the MTT, habenula, and lateral and medial geniculate nuclei were segmented in under 4 minutes. Comparable accuracy with no statistically significant differences in Dice or VSI was achieved for the whole thalamus and 12 thalamic nuclei when comparing 3T and 7T data. A transfer learning approach was employed to incorporate information learnt from a WMn-MPRAGE network to segment thalamic nuclei from CSF-nulled MPRAGE images which have poor intra-thalamic contrast. While the Dice values were slightly lower than corresponding WMn-MPRAGE images acquired on the same patient, even for the smaller nuclei they ranged from 0.62-0.71 (vs. 0.67-0.79 for WMn-MPRAGE) and 0.62-0.82 for larger nuclei (vs. 0.71-0.87 for WMn-MPRAGE).

Previous neuroimaging studies have shown evidence of thalamic involvement in MS albeit confined to the whole thalamus. Planche et al.⁷² recently demonstrated atrophy of specific thalamic nuclei due to MS. Our method showed a statistically significant atrophy in patients with MS compared to healthy subjects for the whole thalamus as well as for AV, VPL, Pul, MGN, and MD nuclei, comporting well with the results of Planche et al.⁷² The antero-ventral nucleus is a critical component in episodic memory and the circuit of Papez. Our network could successfully segment this nucleus with a mean Dice of 0.79 and 0.69 for WMn-MPRAGE and conventional MPRAGE, respectively. The latter is of critical importance for analyzing public databases such as the Alzheimer's disease neuroimaging initiative (ADNI), which only have conventional MPRAGE data, to study the effect of Alzheimer's disease on nuclei such as AV and MD, which are critically involved in episodic memory.

The recent statistical shape model based segmentation of Liu et al.⁷³ is one of the few methods that segment MPRAGE data using the Morel atlas convention. While their method generated 23 nuclei, the lateral and medial geniculate nuclei were notably absent in their output. During manual segmentation, we chose to merge some of the smaller nuclei with larger contiguous nuclei, resulting in the smaller number of reported nuclei compared to their method (e.g. MD is combined with Pf, the pulvinar complex is segmented as a single nucleus in our manual segmentation). Our network results on the WMn-MPRAGE datasets show comparable Dice values for most nuclei, lower Dice for VPL and VA nuclei and higher Dice for CM nucleus and MTT, compared to their shape-based method. However, the network results from conventional MPRAGE datasets showed lower accuracy in comparison, presumably due to the lack of shape information, which could help in the face of poor intra-thalamic contrast. Our analysis had a much larger spread of cases encompassing healthy controls (n=13) as well as patients with ET (n=12) and MS (n=15) compared to 9 healthy subjects in Liu et al. The only other method that has been proposed for thalamic nuclei segmentation using structural imaging is the Bayesian atlas of Iglesias et al.²⁴ We could not directly compare against this method as they do not report Dice values against manual segmentation. Furthermore, their method was optimized for 3T and is very sensitive to bias-field variations which are significant at 7T.

The proposed work has limitations that are common to most deep learning methods. Data diversity during the training phase is critical in creating a generalizable network. The current network was trained using images acquired from multiple field strengths and brain pathologies. The performance of this network on other diseases such as Alzheimer's disease needs to be evaluated. CNN based methods including ours are likely to fail on cases with large artifacts such as metal artifacts from surgical clips or deep brain stimulation electrodes. Limitations specific to our implementation include the use of automatic cropping, which increases the total processing time to segment a dataset from 1 to 4 minutes. This could be avoided by training the network with uncropped images, at the risk of significant increase in memory requirements. Further, with sufficient 3D training data and memory, a 3D cascaded network designed will likely improve the accuracy of our method by fully leveraging the 3D structural information. We also observed a slight reduction in performance in the CSFn-MPRAGE dataset compared to the WMn-MPRAGE dataset for the smaller nuclei. This could partly be due to the inherently lower intra-thalamic contrast in conventional CSFn-MPRAGE. Future work will explore synthesizing WMn-MPRAGE images from conventional MPRAGE using contrast synthesis methods⁸⁹⁻⁹⁰ and then applying the WMn MPRAGE optimized network for better accuracy.

CONCLUSION

We have proposed a CNN based cascaded multi-class multi-planar method for the segmentation of thalamic nuclei and evaluated it on images with different contrasts, and magnetic field strengths for both healthy and diseased populations. The proposed work has successfully applied to both advanced MR acquisition techniques with high intra-thalamic contrast (WMn-MPRAGE) and the more commonly used low intra-thalamic contrast sequences (CSFn-MPRAGE). Further, the effectiveness of the proposed method in real-life applications is investigated via a clinical analysis of volume atrophy in patients with MS.

ACKNOWLEDGEMENTS

We would like to acknowledge funding support from the National Institutes of Health (R21 AA023582-01) and the Arizona Alzheimer's Consortium.

ABBREVIATIONS

AV	Anterior ventral nucleus
CM	Centromedian nucleus
CSF	Cerebrospinal fluid
CSFn	Cerebrospinal fluid nulled
DTI	Diffusion tensor imaging
Hb	Habenular nucleus
LGN	Lateral geniculate nucleus
MD	Mediodorsal nucleus
MGN	Medial geniculate nucleus
MPRAGE	Magnetization-prepared rapid gradient echo
MTT	Mammillothalamic tract
Pul	Pulvinar nucleus
VA	Ventral anterior nucleus
VIM	Ventralis intermedius nucleus
VLa	Ventral lateral anterior nucleus
VLp	Ventral lateral posterior nucleus
VPL	Ventral posterolateral nucleus
WM	White matter
WMn	White matter nulled

REFERENCES

1. Aggleton JP, O'Mara SM, Vann SD, Wright NF, Tsanov M, Erichsen JT. Hippocampal-anterior thalamic pathways for memory: uncovering a network of direct and indirect actions. *Eur. J. Neurosci.* 2010;31(12):2292–2307.
2. Steriade M, Llinás RR. The functional states of the thalamus and the associated neuronal interplay. *Physiol. Rev.* 1988;68(3):649–742.
3. Bodart O, Laureys S, Gosseries O. Coma and disorders of consciousness: scientific advances and practical considerations for clinicians. *Semin. Neurol.* 2013;33(2):83–90.
4. Stein T, Moritz C, Quigley M, Cordes D, Haughton V, Meyerand E. Functional connectivity in the thalamus and hippocampus studied with functional MR imaging. *AJNR Am. J. Neuroradiol.* 2000;21(8):1397–1401.

5. Andreasen NC. The role of the thalamus in schizophrenia. *Can. J. Psychiatry.* 1997;42(1):27–33.
6. Parnaudeau S, Bolkan SS, Kellendonk C. The Mediodorsal Thalamus: An Essential Partner of the Prefrontal Cortex for Cognition. *Biol. Psychiatry.* 2018;83(8):648–656.
7. Arts NJM, Walvoort SJW, Kessels RPC. Korsakoff's syndrome: A critical review. *Neuropsychiatric Disease and Treatment.* 2017.
8. Fama R, Rosenbloom MJ, Sassoon SA, Rohlfing T, Pfefferbaum A, Sullivan E V. Thalamic volume deficit contributes to procedural and explicit memory impairment in HIV infection with primary alcoholism comorbidity. *Brain Imaging and Behavior.* 2014.
9. Benabid AL, Pollak P, Seigneuret E, Hoffmann D, Gay E, Perret J. Chronic VIM thalamic stimulation in Parkinson's disease, essential tremor and extra-pyramidal dyskinesias. *Acta neurochirurgica. Supplementum.* 1993.
10. Minagar A, Barnett MH, Benedict RHB, Pelletier D, Pirko I, Sahraian MA, Frohman E, Zivadinov R. The thalamus and multiple sclerosis: modern views on pathologic, imaging, and clinical aspects. *Neurology.* 2013;80(2):210–219.
11. Braak H, Braak E. Alzheimer's disease affects limbic nuclei of the thalamus. *Acta Neuropathol.* 1991;81(3):261–268.
12. Lee J-Y, Yoon EJ, Lee WW, Kim YK, Lee J-Y, Jeon B. Lateral geniculate atrophy in Parkinson's with visual hallucination: A trans-synaptic degeneration? *Mov. Disord.* 2016;31(4):547–554.
13. Brodkey JA, Tasker RR, Hamani C, McAndrews MP, Dostrovsky JO, Lozano AM. Tremor cells in the human thalamus: differences among neurological disorders. *J. Neurosurg.* 2004;101(1):43–47.
14. Benabid AL, Pollak P, Gao D, Hoffmann D, Limousin P, Gay E, Payen I, Benazzouz A. Chronic electrical stimulation of the ventralis intermedialis nucleus of the thalamus as a treatment of movement disorders. *J. Neurosurg.* 1996;84(2):203–214.
15. Fama R, Sullivan E V. Thalamic structures and associated cognitive functions: Relations with age and aging. *Neurosci. Biobehav. Rev.* 2015;54:29–37.
16. Elias WJ, Huss D, Voss T, Loomba J, Khaled M, Zadicario E, Frysinger RC, Sperling SA, Wylie S, Monteith SJ, et al. A pilot study of focused ultrasound thalamotomy for essential tremor. *N. Engl. J. Med.* 2013;369(7):640–648.
17. Krauth A, Blanc R, Poveda A, Jeanmonod D, Morel A, Székely G. A mean three-dimensional atlas of the human thalamus: generation from multiple histological data. *Neuroimage.* 2010;49(3):2053–2062.

18. Jakab A, Blanc R, Berényi EL, Székely G. Generation of individualized thalamus target maps by using statistical shape models and thalamocortical tractography. *AJNR Am. J. Neuroradiol.* 2012;33(11):2110–2116.
19. Tourdias T, Saranathan M, Levesque IR, Su J, Rutt BK. Visualization of intrathalamic nuclei with optimized white-matter-nulled MPRAGE at 7T. *Neuroimage.* 2014;84:534–545.
20. Fischl B, Salat DH, Busa E, Albert M, Dieterich M, Haselgrove C, van der Kouwe A, Killiany R, Kennedy D, Klaveness S, et al. Whole brain segmentation: automated labeling of neuroanatomical structures in the human brain. *Neuron.* 2002;33(3):341–355.
21. FreeSurfer FB. B. Fischl. *Neuroimage.* 2012;62(2):774–781.
22. Patenaude B, Smith SM, Kennedy DN, Jenkinson M. A Bayesian model of shape and appearance for subcortical brain segmentation. *Neuroimage.* 2011;56(3):907–922.
23. Heckemann RA, Hajnal J V, Aljabar P, Rueckert D, Hammers A. Automatic anatomical brain MRI segmentation combining label propagation and decision fusion. *Neuroimage.* 2006;33(1):115–126.
24. Iglesias JE, Insausti R, Lerma-Usabiaga G, Bocchetta M, Van Leemput K, Greve DN, van der Kouwe A, Alzheimer’s Disease Neuroimaging Initiative, Fischl B, Caballero-Gaudes C, et al. A probabilistic atlas of the human thalamic nuclei combining ex vivo MRI and histology. *Neuroimage.* 2018;183:314–326.
25. Smith SM, Jenkinson M, Woolrich MW, Beckmann CF, Behrens TEJ, Johansen-Berg H, Bannister PR, De Luca M, Drobnjak I, Flitney DE, et al. Advances in functional and structural MR image analysis and implementation as FSL. *NeuroImage.* 2004;23:S208--S219.
26. Haacke EM, Mark Haacke E, Xu Y, Cheng Y-CN, Reichenbach JR. Susceptibility weighted imaging (SWI). *Magnetic Resonance in Medicine.* 2004;52(3):612–618.
27. Abosch A, Yacoub E, Ugurbil K, Harel N. An assessment of current brain targets for deep brain stimulation surgery with susceptibility-weighted imaging at 7 tesla. *Neurosurgery.* 2010;67(6):1745--56; discussion 1756.
28. Xiao Y, Zitella LM, Duchin Y, Teplitzky BA, Kastl D, Adriany G, Yacoub E, Harel N, Johnson MD. Multimodal 7T Imaging of Thalamic Nuclei for Preclinical Deep Brain Stimulation Applications. *Front. Neurosci.* 2016;10:264.
29. Behrens TEJ, Johansen-Berg H, Woolrich MW, Smith SM, Wheeler-Kingshott

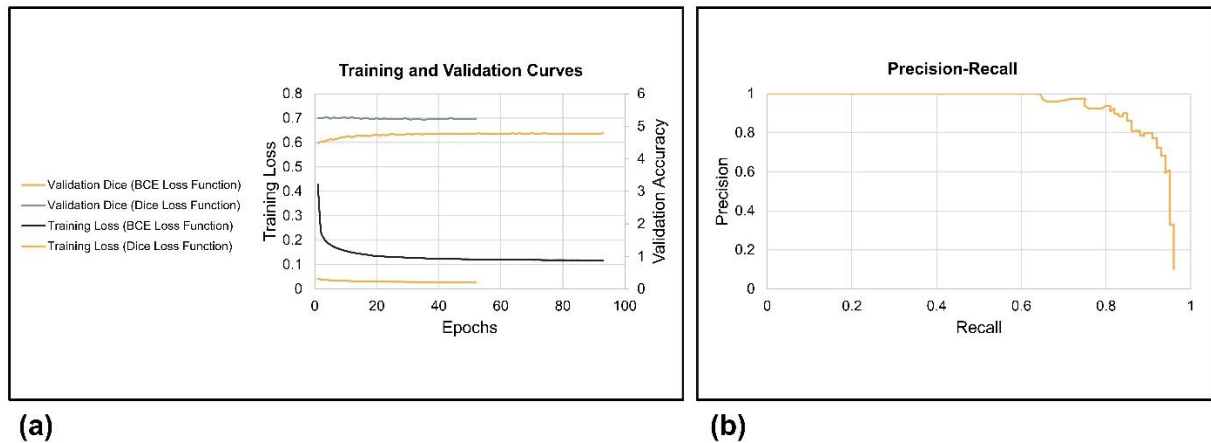
- CAM, Boulby PA, Barker GJ, Sillery EL, Sheehan K, Ciccarelli O, et al. Non-invasive mapping of connections between human thalamus and cortex using diffusion imaging. *Nat. Neurosci.* 2003;6(7):750–757.
30. Wiegell MR, Tuch DS, Larsson HBW, Wedeen VJ. Automatic segmentation of thalamic nuclei from diffusion tensor magnetic resonance imaging. *Neuroimage.* 2003;19(2 Pt 1):391–401.
31. Kumar V, Mang S, Grodd W. Direct diffusion-based parcellation of the human thalamus. *Brain Structure and Function.* 2015.
32. Mang SC, Busza A, Reiterer S, Grodd W, Klose AU. Thalamus segmentation based on the local diffusion direction: A group study. *Magnetic Resonance in Medicine.* 2012.
33. Battistella G, Najdenovska E, Maeder P, Ghazaleh N, Daducci A, Thiran JP, Jacquemont S, Tuleasca C, Levivier M, Bach Cuadra M, et al. Robust thalamic nuclei segmentation method based on local diffusion magnetic resonance properties. *Brain Structure and Function.* 2017.
34. Su JH, Thomas FT, Kasoff WS, Tourdias T, Choi EY, Rutt BK, Saranathan M. Thalamus Optimized Multi Atlas Segmentation (THOMAS): fast, fully automated segmentation of thalamic nuclei from structural MRI. *NeuroImage.* 2019;194:272–282.
35. Stough J V., Ye C, Ying SH, Prince JL. Thalamic parcellation from multi-modal data using random forest learning. In: *Proceedings - International Symposium on Biomedical Imaging.* 2013.
36. Glaister J, Carass A, NessAiver T, Stough J V, Saidha S, Calabresi PA, Prince JL. Thalamus segmentation using multi-modal feature classification: Validation and pilot study of an age-matched cohort. *Neuroimage.* 2017;158:430–440.
37. Van Leemput K. Encoding probabilistic brain atlases using Bayesian inference. *IEEE Trans. Med. Imaging.* 2009;28(6):822–837.
38. Iglesias JE, Augustinack JC, Nguyen K, Player CM, Player A, Wright M, Roy N, Frosch MP, McKee AC, Wald LL, et al. A computational atlas of the hippocampal formation using ex vivo, ultra-high resolution MRI: Application to adaptive segmentation of in vivo MRI. *Neuroimage.* 2015;115:117–137.
39. Vassal F, Coste J, Derost P, Mendes V, Gabrillargues J, Nuti C, Durif F, Lemaire J-J. Direct stereotactic targeting of the ventrointermediate nucleus of the thalamus based on anatomic 1.5-T MRI mapping with a white matter attenuated inversion recovery (WAIR) sequence. *Brain Stimulation.* 2012;5(4):625–633.

40. Sudhyadhom A, Haq IU, Foote KD, Okun MS, Bova FJ. A high resolution and high contrast MRI for differentiation of subcortical structures for DBS targeting: the Fast Gray Matter Acquisition T1 Inversion Recovery (FGATIR). *Neuroimage*. 2009;47 Suppl 2:T44--52.
41. Alvéén J. Improving Multi-atlas Segmentation Methods for Medical Images. Department of Signals and Systems, Chalmers University of Technology; 2017.
42. Wang J, Vachet C, Rumpel A, Gouttard S, Ouziel C, Perrot E, Du G, Huang X, Gerig G, Styner M. Multi-atlas segmentation of subcortical brain structures via the AutoSeg software pipeline. *Front. Neuroinform*. 2014;8:7.
43. Liu Y, D'Haese P-F, Newton AT, Dawant BM. Thalamic nuclei segmentation in clinical 3T T1-weighted Images using high-resolution 7T shape models. In: *Medical Imaging 2015: Image-Guided Procedures, Robotic Interventions, and Modeling*. Vol. 9415. International Society for Optics and Photonics; 2015. p. 94150E.
44. Brebisson A de, de Brebisson A, Montana G. Deep neural networks for anatomical brain segmentation. 2015 IEEE Conference on Computer Vision and Pattern Recognition Workshops (CVPRW). 2015.
45. Jia H, Xia Y, Cai W, Fulham M, Feng DD. Prostate segmentation in MR images using ensemble deep convolutional neural networks. 2017 IEEE 14th International Symposium on Biomedical Imaging (ISBI 2017). 2017.
46. Chen Y, Shi B, Wang Z, Sun T, Smith CD, Liu J. Accurate and Consistent Hippocampus Segmentation Through Convolutional LSTM and View Ensemble. *Machine Learning in Medical Imaging*. 2017:88–96.
47. Moeskops P, Viergever MA, Mendrik AM, de Vries LS, Benders MJNL, Isgum I. Automatic Segmentation of MR Brain Images With a Convolutional Neural Network. *IEEE Trans. Med. Imaging*. 2016;35(5):1252–1261.
48. Guo Y, Liu Y, Oerlemans A, Lao S, Wu S, Lew MS. Deep learning for visual understanding: A review. *Neurocomputing*. 2016;187:27–48.
49. Ram S, Majdi MS, Rodriguez JJ, Gao Y, Brooks HL. Classification of primary cilia in microscopy images using convolutional neural random forests. In: *Proceedings of the IEEE Southwest Symposium on Image Analysis and Interpretation*. 2018.
50. Zhu H, Shi F, Wang L, Hung S-C, Chen M-H, Wang S, Lin W, Shen D. Dilated Dense U-Net for Infant Hippocampus Subfield Segmentation. *Front. Neuroinform*. 2019;13:30.
51. Shakeri M, Tsogkas S, Ferrante E, Lippe S, Kadoury S, Paragios N, Kokkinos I.

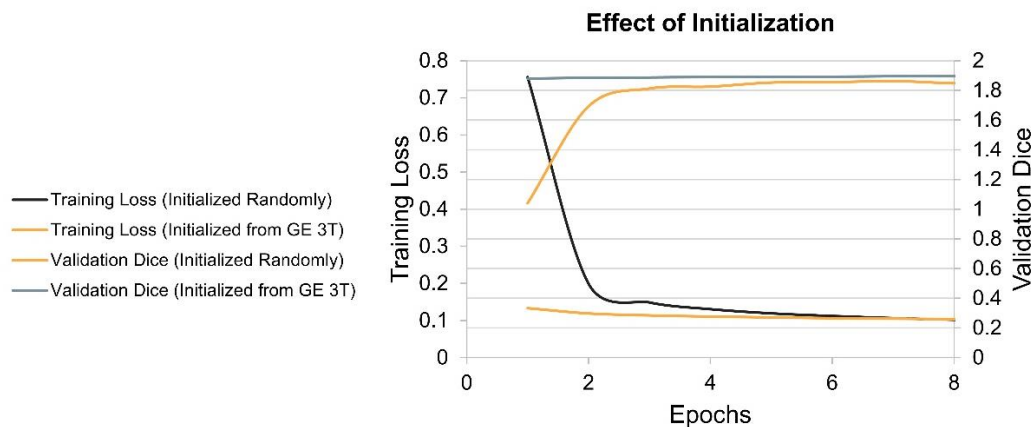
- Sub-cortical brain structure segmentation using F-CNN'S. 2016 IEEE 13th International Symposium on Biomedical Imaging (ISBI). 2016.
52. Milletari F, Ahmadi S-A, Kroll C, Plate A, Rozanski V, Maiostre J, Levin J, Dietrich O, Ertl-Wagner B, Bötzel K, et al. Hough-CNN: Deep Learning for Segmentation of Deep Brain Regions in MRI and Ultrasound. 2016 Jan.
53. Kushibar K, Valverde S, González-Villà S, Bernal J, Cabezas M, Oliver A, Lladó X. Automated sub-cortical brain structure segmentation combining spatial and deep convolutional features. *Med. Image Anal.* 2018;48:177–186.
54. Prason A, Petersen K, Igel C, Lauze F, Dam E, Nielsen M. Deep feature learning for knee cartilage segmentation using a triplanar convolutional neural network. In: *Lecture Notes in Computer Science (including subseries Lecture Notes in Artificial Intelligence and Lecture Notes in Bioinformatics)*. 2013.
55. Roth HR, Lu L, Seff A, Cherry KM, Hoffman J, Wang S, Liu J, Turkbey E, Summers RM. A new 2.5D representation for lymph node detection using random sets of deep convolutional neural network observations. In: *Lecture Notes in Computer Science (including subseries Lecture Notes in Artificial Intelligence and Lecture Notes in Bioinformatics)*. 2014.
56. Tajbakhsh N, Shin JY, Gurudu SR, Hurst RT, Kendall CB, Gotway MB, Jianming Liang. Convolutional Neural Networks for Medical Image Analysis: Full Training or Fine Tuning? *IEEE Trans. Med. Imaging.* 2016;35(5):1299–1312.
57. Saranathan M, Tourdias T, Bayram E, Ghanouni P, Rutt BK. Optimization of white-matter-nulled magnetization prepared rapid gradient echo (MP-RAGE) imaging. *Magn. Reson. Med.* 2015;73(5):1786–1794.
58. Ioffe S, Szegedy C. Batch Normalization: Accelerating Deep Network Training by Reducing Internal Covariate Shift. 2015 Feb.
59. Srivastava N, Hinton G, Krizhevsky A, Sutskever I, Salakhutdinov R. Dropout: a simple way to prevent neural networks from overfitting. *J. Mach. Learn. Res.* 2014;15(1):1929–1958.
60. Ronneberger O, Fischer P, Brox T. U-Net: Convolutional Networks for Biomedical Image Segmentation. In: *Medical Image Computing and Computer-Assisted Intervention -- MICCAI 2015*. Springer International Publishing; 2015. p. 234–241.
61. He K, Zhang X, Ren S, Sun J. Deep residual learning for image recognition. In: *Proceedings of the IEEE conference on computer vision and pattern recognition*. 2015. p. 770–778.

62. Maas AL, Hannun AY, Ng AY. Rectifier nonlinearities improve neural network acoustic models. In: Proc. icml. Vol. 30. 2013. p. 3.
63. Novikov AA, Lenis D, Major D, Hladuvka J, Wimmer M, Buhler K. Fully Convolutional Architectures for Multiclass Segmentation in Chest Radiographs. *IEEE Trans. Med. Imaging*. 2018;37(8):1865–1876.
64. Crum WR, Camara O, Hill DLG. Generalized overlap measures for evaluation and validation in medical image analysis. *IEEE Trans. Med. Imaging*. 2006;25(11):1451–1461.
65. Drozdal M, Vorontsov E, Chartrand G, Kadoury S, Pal C. The Importance of Skip Connections in Biomedical Image Segmentation. 2016 Aug.
66. Kingma DP, Ba J. Adam: A Method for Stochastic Optimization. 2014 Dec.
67. Niemann K, Mennicken VR, Jeanmonod D, Morel A. The Morel stereotactic atlas of the human thalamus: atlas-to-MR registration of internally consistent canonical model. *Neuroimage*. 2000;12(6):601–616.
68. Chollet F. Keras (2015). URL <http://keras.io>. 2017.
69. Dice LR. Measures of the Amount of Ecologic Association Between Species. *Ecology*. 1945;26(3):297–302.
70. Karimi D, Salcudean SE. Reducing the Hausdorff Distance in Medical Image Segmentation with Convolutional Neural Networks. *IEEE Transactions on Medical Imaging*. 2019.
71. Taha AA, Hanbury A. An Efficient Algorithm for Calculating the Exact Hausdorff Distance. *IEEE Transactions on Pattern Analysis and Machine Intelligence*. 2015.
72. Planche V, Su JH, Mournet S, Saranathan M, Dousset V, Han M, Rutt BK, Tourdias T. White-matter-nulled MPRAGE at 7T reveals thalamic lesions and atrophy of specific thalamic nuclei in multiple sclerosis. *Multiple Sclerosis Journal*. 2019.
73. Liu Y, D'Haese PF, Newton AT, Dawant BM. Generation of human thalamus atlases from 7 T data and application to intrathalamic nuclei segmentation in clinical 3 T T1-weighted images. *Magnetic Resonance Imaging*. 2020.

Supporting Materials



Supporting Figure S1: **a)** Effect of loss function on training and validation curves are shown. We can see a faster convergence along with higher validation accuracy for Dice based loss function in comparison to BCE loss function. **b)** the precision-recall curve for one of the WMn-MPRAGE test subjects is shown.



Supporting Figure S2: The effect of initialization on final accuracy and convergence curves - The validation accuracy (Dice) and training loss w/o network initialization from a network trained on the GE 3T dataset is shown. The segmentation results indicate a statistically significant improvement over two nuclei (VA, and Hb) in the presence of initialization from GE 3T network.

Supporting Table S1: Imaging acquisition parameters for WMn- and CSFn-MPRAGE for 7T and 3T data used in this study

	WMn-MPRAGE		CSFn-MPRAGE
scanner	3T (GE)	7T (GE)	7T (GE)
TR/TS (ms)	10/4500	10/6000	7.2/3000
TI (ms)	500	680	1200
Flip (deg)	9	4	6
Matrix	180 × 180 × 220	180 × 180 × 220	180 × 180 × 220
Slice thickness (mm)	1	1	1
Parallel imaging	None	1.5 × 1.5	3x1
Coil	8-channel GE	32-channel Nova	32-channel Nova

Supporting Table S2: Effect of freezing different layers on Dice coefficients for CSFn-MPRAGE datasets

	Last layer	Last 2 layer	Top layer	Left top layer	Left top 2 layers	Right top layer	Right top 2 layers	Left top 2 and top right layers	Full fine tune
THALAMUS	0.87	0.88	0.88	0.84	0.88	0.85	0.86	0.88	0.88
Pul	0.76	0.79	0.79	0.77	0.77	0.75	0.77	0.79	0.79
VLP	0.74	0.76	0.76	0.76	0.77	0.72	0.74	0.76	0.74
MD-Pf	0.78	0.78	0.81	0.81	0.80	0.77	0.79	0.81	0.80
VPI	0.52	0.58	0.60	0.54	0.55	0.52	0.47	0.57	0.54
VA	0.64	0.69	0.71	0.72	0.70	0.66	0.69	0.71	0.67
LGN	0.64	0.60	0.64	0.64	0.65	0.56	0.62	0.65	0.64
AV	0.63	0.64	0.63	0.66	0.63	0.60	0.63	0.63	0.65
CM	0.53	0.59	0.60	0.61	0.61	0.58	0.56	0.63	0.65
VLa	0.57	0.62	0.65	0.60	0.63	0.51	0.59	0.67	0.61
MGN	0.60	0.60	0.61	0.66	0.62	0.60	0.65	0.63	0.61
MTT	0.58	0.49	0.55	0.53	0.55	0.52	0.47	0.55	0.54
Hb	0.68	0.69	0.71	0.70	0.69	0.71	0.70	0.70	0.71

Supporting Table S3: Comparison of Hausdorff distance for THOMAS vs. proposed CNN-based method for healthy controls and MS for WMn-MPRAGE and CSFn-MPRAGE

Contrast	WMn				CSFn	
	Control 7T		MS 7T		Control 7T	MS 7T
Method	THOMAS (n=13)	CNN (n=13)	THOMAS (n=15)	CNN (n=15)	CNN (n=7)	CNN (n=15)
THALAMUS	2.55	2.50	2.84	2.73*	2.91	2.92
Pul	1.77	1.74	1.95	1.81*	2.19	2.10
VLp	2.05	2.05	2.22	2.21	2.32	2.35
MD-Pf	2.10	2.12	2.31	2.31	2.55	2.52
VPL	1.76	1.81	1.82	1.88	2.32	2.17
VA	1.86	1.77*	2.01	1.92*	1.97	2.02
LGN	1.90	1.95	2.07	2.11	2.28	2.20
AV	1.77	1.80	1.82	1.88	2.01	2.18
CM	1.85	1.83	1.93	1.89	2.10	2.00
VLa	1.71	1.74	1.84	1.87	2.04	2.17
MGN	1.26*	1.35	1.23	1.33	1.60	1.58
MTT	0.97	0.96	1.13	1.14	1.46	1.44
Hb	1.16	1.07	1.30	1.19*	1.28	1.36

* p < 0.05 CNN vs. THOMAS